

Oxygen Reduction on Pd_{0.75}Co_{0.25} (111) and Pt_{0.75}Co_{0.25} (111) Surfaces: An ab Initio Comparative Study

Eduardo J. Lamas and Perla B. Balbuena*

Department of Chemical Engineering, Texas A&M University,
College Station, Texas 77843

Received June 17, 2006

Abstract: Density functional theory studies of adsorption of oxygen electroreduction intermediates and free energy profiles are used to discuss possible reaction mechanisms: one leading directly to H₂O production and another having H₂O₂ as an intermediate, on (111) surfaces of pure Pt, pure Pd, and bimetallic systems Pd_{0.75}Co_{0.25} and Pt_{0.75}Co_{0.25}. It is found that the calculated affinities toward the different ORR intermediates in the studied surfaces follow the Hammer-Norskov d-band model predictions. The calculated free energy profiles and the magnitude of the barriers in both mechanisms seem to favor the hypothesis that both the direct and series O₂ reduction mechanisms might be operating in parallel. The highest thermodynamic barriers at 1/4 of a monolayer atomic oxygen coverage and without solvent are located in the first hydrogenation reaction for both mechanisms.

1. Introduction

In the past few years the quest toward a hydrogen-based economy has intensified the interest for effective and less expensive catalysts for fuel cell applications. Due to its slow kinetics alternative catalysts for the oxygen electroreduction reaction (OERR) are actively researched. Platinum alloys with different transition metals (for example: Ni, Co, and Fe) have shown improved activity over pure Pt.^{1–3} The design of a Pt-free catalyst is also highly desirable, and different alternatives including metalloporphyrins⁴ and Pd-based catalysts are being researched.^{5–7} Pd-based catalysts constitute an attractive alternative to Pt alloys in fuel cell applications, not only because of lower costs but also because of the lower reactivity of Pt alloys toward methanol, which is important for improved methanol crossover tolerance on direct methanol fuel cells.⁸

The oxygen electroreduction reaction and its intermediates have been the object of intensive theoretical^{9–14} and experimental studies.^{1,2,15,16} The important role of OH adsorption on the catalyst surface has been identified; OH bonds strongly to the surface and has a tendency to accumulate on the surfaces that slows down the OERR kinetics by occupying active sites on the catalyst.¹⁷

The Hammer-Norskov d-band model¹⁸ that successfully explains reactivity trends on transition-metal surfaces is a key contribution to the understanding of the main electronic structure characteristics of the surface atoms and their reactivity with adsorbates. This concept, together with Sabatier's principle,¹⁹ can help to perform a rapid screening of candidate catalysts. Sabatier's principle states that the reactivity of a surface should reach a compromise between having enough strength to break bonds and generate the intermediates but low enough interaction not to stabilize them on the surface in order for the catalyst to be efficient on improving the reaction kinetics.

Recently, Norskov^{20,21} proposed an approach for including the cell potential where the Gibbs free energy for the half-cell reactions are derived from density functional theory (DFT) calculations and thermodynamic data; this method is applied in this work to obtain free energy profiles at the cell equilibrium potential. We report the analyses of two possible oxygen electroreduction mechanisms on Pt- and Pd-based alloys and the interaction of the OERR intermediates with selected transition-metal surfaces.

In this work, the hydration effect of intermediates on adsorption energies and free energy profiles was not included. The effect of water in the overall reaction, its similarities and differences among the different catalysts, changes in

* Corresponding author e-mail: balbuena@tamu.edu.

Table 1. Transferability Tests for the Pd Pseudopotential^a

state	<i>E</i> all electron (Ry)	<i>E</i> pseudo (Ry)	diff (Ry)
4d10	−0.297504	−0.297505	0.000001
5s0	−0.24414	−0.24414	0.000000
5p0	−0.023	−0.023	0.000000
4d9.75	−0.342907	−0.343394	0.000487
5s0.25	−0.262584	−0.262315	−0.000269
5p0	−0.032494	−0.032367	−0.000127
4d9	−0.564201	−0.568206	0.004005
5s0.5	−0.370635	−0.370208	−0.000427
5p0.5	−0.095426	−0.095157	−0.000269
4d9	−0.491517	−0.495178	0.003661
5s1	−0.320069	−0.319349	−0.00072
5p0	−0.058215	−0.057809	−0.000406

^a The last column provides the difference between the energies from the pseudopotential and those of a full electron calculation for the various states in column 1.

adsorption energies, and effects in the overall reaction will be addressed in future work where the results will also be contrasted with the ones here presented.

2. Methodology

DFT calculations of the oxygen reduction reaction intermediates were performed on Pt, Pd, Pd_{0.75}Co_{0.25}, and Pt_{0.75}Co_{0.25} using the plane wave framework. The unit cell is modeled as a three-layer — 4 atoms per layer (111) surfaces. In the bimetallic case, we studied two skin systems with the same Co distributions on Pt-based and Pd-based systems; in both cases the proportions of Co are 0% in the first layer, 50% in the second layer, and 25% in the third layer. Periodic boundary conditions are applied in the three spatial directions, and 10 Å of vacuum space is left between periodic images in the direction perpendicular to the surface.

We adopted Vanderbilt ultrasoft pseudopotentials²² to decrease the computational requirements associated with the description of inert core electrons, together with the PBE exchange correlation functional. All pseudopotentials are either obtained from Vanderbilt's library²³ or derived from that reference. The Pd pseudopotential is based on a Rh pseudopotential available in the library and developed by Hansen designed with 2 s, 2 p, and 2 d nonlocal projectors and nonlinear core correction (rcloc = 2.2 au); the cut off radii are set to rc = 2.64 au for the s and p channels, and rc = 1.55 au for the d channel. In all cases transferability is verified; the results for Pd are shown in Table 1, and this pseudopotential gives a cell constant expanded nearly 1% with respect to experimental results with $a_0 = 3.926$ Å. The plane wave cut off is set to 50 Ry, and the first Brillouin zone is sampled with a Monkhorst Pack mesh with $7 \times 7 \times 1$ k-points. To facilitate convergence, fractional occupancies are allowed applying the Mazzari-Vanderbilt cold smearing scheme.²⁴ The electronic temperature is set to 1000 K, with a smearing parameter of $kT \sim 0.0325$ eV.

The geometries of the different species in this study are relaxed using the Broyden-Fletcher-Goldfarb-Shanno (BFGS)^{25–28} method ensuring that residual forces are below 10^{-3} Ry/au and with a change in total energy under 10^{-4} Ry between BFGS steps. The wave functions are converged in such a way that energy changes are under 10^{-6} Ry during

self-consistent iterations; in all cases the calculations include spin polarization, and the nonzero magnetization states are taken into account in the Co alloys. All these convergence criteria are verified by running a few calculations with tighter convergence parameters and checking geometries and energies against the data obtained with the above-mentioned parameters.

In all cases the adsorption energy is calculated according to

$$\Delta E = \frac{1}{n}(E_{S+nA} - (E_S - n \cdot E_A)) \quad (1)$$

where *S* is the clean surface, *A* is the adsorbate, and *n* is the number of adsorbate molecules in the unit cell.

The changes in electron density originated by the surface–adsorbate interactions have been calculated according to

$$\Delta\rho(\vec{x}) = \rho(\vec{x})_{s+ads} - (\rho(\vec{x})_s + \rho(\vec{x})_{ads}) \quad (2)$$

To gain understanding into the reactivity potential of the different studied surfaces, the local density of states is calculated by projecting the plane wave expansion into a linear combination of atomic orbitals. All simulations and data analysis were performed with the pw.x program and postprocessing utilities that are part of the quantum ESPRESSO package.²⁹ The visualizations were obtained with VMD.³⁰

3. Surface Characterization

After alloying, surface properties can be generally affected in many different ways. Succinctly these changes can be classified as electronic (for example, band shifting due to the presence of a second component) and structural such as one component island formation, skin formation, and/or lattice constant changes. These changes are also entangled; for example, a change in the lattice constant will also generate a change in the system's band structure. In this section, we discuss some of the studied alloy characteristics focusing mainly on the lattice constant and d-band structure changes that, as mentioned in the introductory section, have proven of capital importance in the characterization of transition-metal catalysts.

The surfaces studied in this work have their lattice constants for pure Pt and Pd fixed to their experimental values (3.92 Å and 3.89 Å, respectively), while their Co-alloys lattice constants are estimated from variable cell calculations using the Wentzcovitch damped dynamics algorithm.³¹ In all cases where Co is present we found a lattice contraction with final lattice constant $a_0 = 3.85$ Å for the PdCo alloy and $a_0 = 3.89$ Å in the PtCo alloy in good agreement with previously published data (Xu et al.¹⁴ calculation yielded 3.85 Å for the same PtCo alloy). The PdCo and PtCo alloys are found to be magnetic in their ground states, whereas the Pt and Pd surfaces are restricted to the nonmagnetic state during the calculations (see ref 32 for an extended discussion on magnetization issues associated with modeling Pd systems).

Figure 1 shows the localized density of states vs the energy (referred to the Fermi level of the metal or alloy calculated

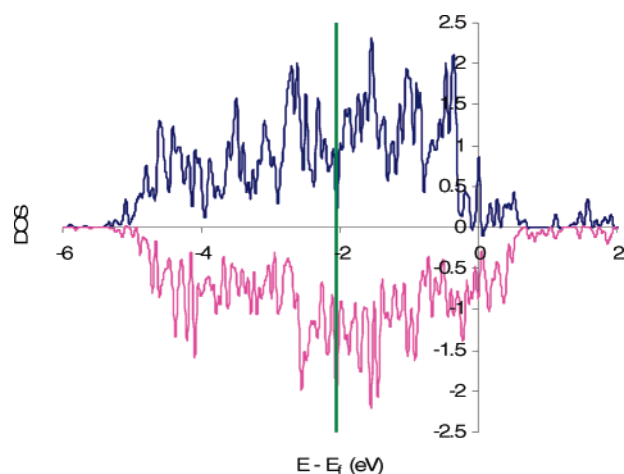


Figure 1. d-Band density of states for surface Pd atoms in the $\text{Pd}_{0.75}\text{Co}_{0.25}$ alloy. The d-band center (averaged for the spin up and down states) is also shown in the figure (green line). The positive intensities correspond to states of spin-up, and the negatives to spin-down.

by the model) of the d-band in the surface Pd atoms of the skin $\text{Pd}_{0.75}\text{Co}_{0.25}$ (111) alloy. The location of the first moment of the d-band structure (the d-band center) is also indicated in the picture. The d-band center is located 2.06 eV below the Fermi level in the $\text{Pd}_{0.75}\text{Co}_{0.25}$ surface, 1.88 eV for the

Pd surface, 2.36 eV for Pt, and 2.49 eV for $\text{Pt}_{0.75}\text{Co}_{0.25}$. If the d-band model holds for these metals the strengths of the adsorbate–surface interactions should be in increasing order: $\text{PtCo} < \text{Pt} < \text{PdCo} < \text{Pd}$; an analysis of adsorption energy values in Tables 2–6 shows that the agreement is indeed excellent.

4. Oxygen Electroreduction Intermediates and Their Interactions with Transition-Metal Surfaces

4.1. Atomic and Molecular Oxygen. Oxygen dissociation on Pt (111) is a thermally activated process that occurs above 150 K and evolves through chemical adsorbed precursors. The existence of these precursors has been verified both experimentally and theoretically.³³ Our studies of O_2 on the different surfaces are in agreement with the existence of these precursors. Local minima on the potential energy surface were found with initial configurations of O_2 parallel to the surface, while the studied vertical orientation is not bounded to the surface. The reference calculation for oxygen in the gas phase yielded a triplet as the most stable electronic structure with a O–O bonding distance of 1.23 Å and dissociation energy of 5.81 eV. Figure 2b shows O_2 adsorbed on the Pd skin surface of the $\text{Pd}_{0.75}\text{Co}_{0.25}$ alloy as well as changes on electron density upon adsorption. It is observed

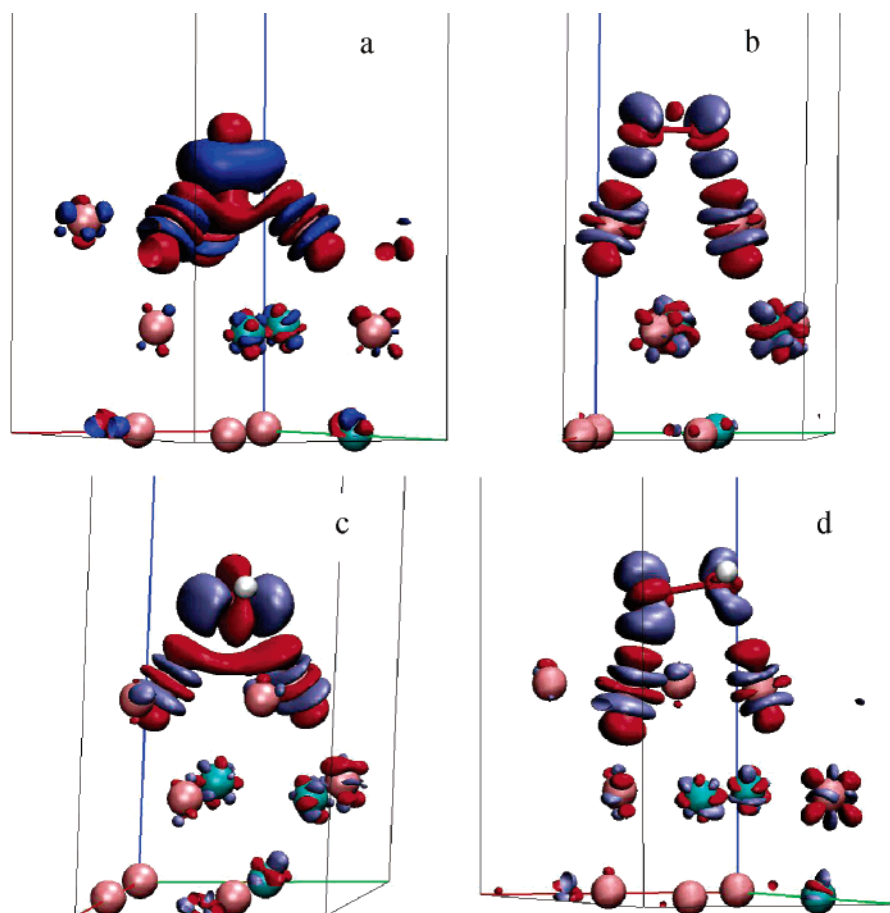


Figure 2. Electron density differences upon adsorption calculated according to eq 2, for (a) atomic oxygen, (b) molecular oxygen, (c) hydroxyl, and (d) hydroperoxyl on the $\text{Pd}_{0.75}\text{Co}_{0.25}$ (111) surface. Pd atoms are in pink, Co atoms are in light blue, oxygen are in red and hydrogen in white. Positive electron density differences are in ice blue, and negative electron density differences are in red. $\Delta\rho$ isosurfaces were calculated at $\pm 0.006 \text{ e/au}^3$.

Table 2. DFT Calculated Molecular Oxygen Adsorption Energies^a

system	ΔE (eV)	distances (Å)		
		O1–M1	O2–M2	O–O
Pt–O ₂	–0.431	2.06	2.07	1.37
Pt _{0.75} Co _{0.25} –O ₂	–0.216	2.14	2.17	1.33
Pd _{0.75} Co _{0.25} –O ₂	–0.408	2.07	2.08	1.33
Pd–O ₂	–0.715	2.01	2.02	1.35

^a The distance between the closest metal atom to each oxygen is tabulated together with the O–O bond distance.

Table 3. DFT Calculated Oxygen Adsorption Energies and Distances^a

system (site)	ΔE (eV)	distances (Å)		
		O–M1	O–M2	O–M3
Pt–O (fcc hollow)	–3.727	2.08	2.08	2.08
Pt–O (hcp hollow)	–3.316	2.11	2.11	2.11
Pt–O (top)	–2.492	1.87		
Pt _{0.75} Co _{0.25} –O (fcc hollow)	–3.490	2.1	2.1	2.09
Pt _{0.75} Co _{0.25} –O (hcp Co-hollow)	–2.995	2.13	2.14	2.09
Pt _{0.75} Co _{0.25} –O (hcp hollow)	–2.855	2.09	2.09	2.15
Pd _{0.75} Co _{0.25} –O (fcc hollow)	–3.778	2.02	2.02	2.03
Pd _{0.75} Co _{0.25} –O (hcp Co-hollow)	–3.473	2.03	2.03	2.01
Pd _{0.75} Co _{0.25} –O (hcp hollow)	–3.464	2.01	2.02	2.03
Pd–O (fcc hollow)	–4.153	1.99	1.99	1.99
Pd–O (hcp hollow)	–3.962	2.01	2.01	2.01
Pd–O (top)	–2.646	1.8		

^a In the hollow cases we report the distances to the three closest surface metal atoms.

that there is a decrease in the electron density in the O–O bond region and an electron flow from the surface to the antibonding π states of each O atom. Qualitatively similar changes in the electronic density upon O₂ adsorption are obtained for a Pt(111) surface; these observations are in excellent agreement with previously reported calculations on a Pt surface.³⁴ The bond elongations signaling the weakening of the O–O bond in all studied surfaces are indicated in Table 2, and the value of 1.37 Å is in good agreement with experimental reports of the superoxo state on Pt(111) surfaces.³⁵

In all surfaces in this study, the preferred adsorption site for atomic oxygen is found to be the *fcc* hollow site (in good agreement with previously reported results³⁶), followed by *hcp* hollow, and then the top site (Table 3). O adsorbed on a top site becomes unstable in the alloy surfaces; in all cases it is found that it slips to a neighbor *hcp* hollow position with an underlying Co atom in the second layer of the surface. The energetic differences between adsorption in both hollow sites (and thus the barriers for O surface diffusion) are also altered by the presence of the second layer Co atoms; in fact, in both alloys this difference is higher than that of the pure metal, going from 0.411 eV in pure Pt to 0.635 eV in the Pt_{0.75}Co_{0.25} alloy and from 0.192 eV on Pd to 0.314 eV in the Pd_{0.75}Co_{0.25} alloy. Due to the strong O-metal bonding, the changes in electron density depicted in Figure 2a are the most dramatic among the different adsorbates showing increased electronic density along a plane parallel to the surface and depleted electronic density along a line

Table 4. DFT Calculated Hydroxyl Adsorption Distances and Energies^a

system (site)	ΔE (eV)	distances (Å)		
		O–M1	O–M2	O–M3
Pt–OH (top)	–2.081	2.02		
Pt–OH (bridge)	–1.989	2.22	2.21	
Pt _{0.75} Co _{0.25} –OH (top)	–1.870	2.05		
Pt _{0.75} Co _{0.25} –OH (bridge)	–1.791	2.24	2.27	
Pd _{0.75} Co _{0.25} –OH (top)				
Pd _{0.75} Co _{0.25} –OH (bridge)	–2.199	2.19	2.17	
Pd–OH (top)	–2.173	1.97		
Pd–OH (bridge)	–2.357	2.14	2.13	

^a In the bridge adsorption cases the reported distances are the two closest surface metal atoms.

Table 5. DFT Calculated HO₂ Adsorption Distances and Energies^a

system	ΔE (eV)	distances (Å)		
		O1–M1	O2–M2	O–O
Pt–HO ₂	–1.043	2.86	2.06	1.43
Pt _{0.75} Co _{0.25} –HO ₂	–0.881	2.9	2.08	1.43
Pd _{0.75} Co _{0.25} –HO ₂	–0.973	2.41	2.04	1.46
Pd–HO ₂	–1.218	2.32	2.01	1.47

^a The last column shows the O–O distance in the adsorbate.

perpendicular to the surface and changes on the surface metal atoms along the metal–adsorbate bonds. These features remain essentially present for all the adsorbates (symmetry axes for the electronic density changes parallel and perpendicular to the surface for the adsorbate and along the metal–adsorbate bonds).

4.2. Hydroxyl (OH). OH is perhaps one the most important OERR intermediates; experimental evidence suggests that it adsorbs strongly on the catalyst surface blocking active sites,³ and its degree of interaction with different transition-metal surfaces is an important indication of their efficiency toward oxygen reduction.

From these calculations it was observed that in Pt-based surfaces the preferred adsorption site is on top, while the preferred adsorption site is a bridge for Pd surfaces. The top site is no longer stable on the Pd atoms of the Pd_{0.75}Co_{0.25} alloy (as in the atomic oxygen case, the OH placed on top slips to neighbor bridge sites), and the adsorbate is slightly displaced from the top position in Pt_{0.75}Co_{0.25}. Energies and bond distances are provided in Table 4.

Figure 2c shows the geometry and electronic changes for OH adsorbed on the Pd surface of the Pd_{0.75}Co_{0.25} alloy. Qualitatively the changes in electronic density are similar to those of the adsorbed atomic oxygen (Figure 2a), although less dramatic changes due to its lower binding strength with the surface.

At a higher OH concentration (half of an OH monolayer obtained as a product of the H₂O₂ dissociation on the surfaces), a hydrogen bond is formed between adsorbed neighbor OH species. This effect further stabilizes the hydroxyl groups giving adsorption energies per OH that are lower than at the low coverage by an amount close to the hydrogen bonding energy in water (23.3 kJ/mol or about 0.24

Table 6. DFT Calculated H₂O₂ Dissociation into Two Adsorbed OH Radicals^a

system (site 1-site 2)	$\Delta E^{(1)}$ (eV)	$\Delta E^{(2)}$ (eV)	distances (Å)				H-bond dist (Å)
			O1–M1	O2–M2	O2–M3	O2–M4	
Pt–2OH(top-top)	–2.056	–2.294	2.02	2.02			1.87
Pt _{0.75} Co _{0.25} –2OH (top-top)	–1.668	–2.100	2.04	2.04			1.78
Pd _{0.75} Co _{0.25} –2OH (top-top)	–1.795	–2.163	2	1.99			1.85
Pd _{0.75} Co _{0.25} –2OH (top-hollow)	–1.777	–2.154	2.01	2.09	2.31	2.74	2.14
Pd–2OH (top-top)	–2.144	–2.338	1.97	1.97			1.95

^a $\Delta E^{(1)}$ is the binding energy calculated according to eq 1 with $n = 1$ and taking $E_{\text{H}_2\text{O}_2}$ as E_{A} , whereas $\Delta E^{(2)}$ is calculated with $n = 2$ and E_{OH} as E_{A} . The values of $\Delta E^{(2)}$ may be compared with those in Table 4 to quantify the stabilization due to hydrogen bonding. The last column in this table gives the hydrogen bonding distance between neighbor hydroxyls.

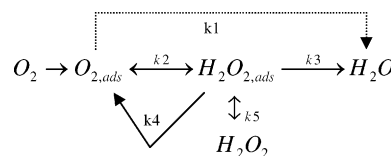
eV see for example ref 37); Table 6 displays binding energies and geometries for the case of 0.5 monolayer OH adsorbed.

4.3. Hydroperoxyl (HO₂). In all the calculated Pt- and Pd-skin cases HO₂ is stable, and no dissociated form is found when starting from an undissociated initial condition. To calculate the binding energies, the HO₂ radical is taken as a reference in the gas phase, with a O–O bonding distance of 1.35 Å, O–H distance of 0.99 Å, and O–O–H angle of 104.96°. After adsorption, the molecule tilts on top of two metal atoms; this tilting is due to the weaker interaction of the OH side of the molecule with the surface. The adsorption energies are listed in Table 5, and Figure 2d shows the geometry over the Pd surface of the Pd_{0.75}Co_{0.25} alloy and an isosurface of the electron density difference calculated according to eq 2. Not surprisingly, in this case, the features of the $\Delta\rho$ plot (Figure 2d) are comparable to the O₂ case; that is, there is an electron density gain in the antibonding π orbital associated with each oxygen atom (this gain is lower in the extreme of the molecule that bonds to hydrogen because of the stability of the O–H covalent bond).

4.4. Hydrogen Peroxide (H₂O₂). The most stable electronic configuration for H₂O₂ is a singlet with bond lengths 1.47 Å for O–O and 0.98 Å for O–H, angles about 100° for H–O–O, and a dihedral angle about 112°. When placed over a surface at about 2 Å, in its vacuum configuration, dissociation is observed in all cases whereas when placed above 2.6 Å, the molecule adsorbs without dissociation tilted with one of its oxygen atoms over a top position. Dissociation energies are reported in Table 6. Once dissociated, two OH species are observed in two possible configurations: one where both OH radicals are adsorbed on top of metal atoms and another where one OH adsorbs on top while the other is in a near-hollow position. On the Pd surface of the Pd_{0.75}Co_{0.25} alloy, a top-top configuration seems to be slightly preferred (Table 6); others reported similar results on Pt(111).³⁸ In both cases, the adsorbed OH rotates forming a hydrogen bond with its neighbor adsorbed OH. The hydrogen bond distances are also reported in Table 6.

5. Free Energy Profiles

Oxygen electroreduction in acidic media can evolve through one or a combination of two different paths; a *direct* pathway that involves O–O bond breaking before a second proton is attached to the molecule and a *series* pathway that generates hydrogen peroxide as an intermediate. Schematically these two pathways are shown in Scheme 1.^{1,39}

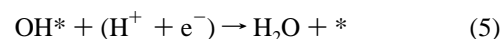
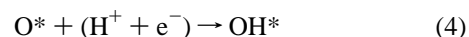
Scheme 1. Two Possible OERR Mechanisms According to Wroblewa et al.^{39 a}

^a The k_i values are the kinetic rate constants associated with each process. The process associated with k_1 is the direct mechanism, whereas the series mechanism involves the formation of adsorbed H₂O₂ (rate constants k_2 and k_3).

In this section we study—via generation of free energy profiles—two representative mechanisms of the OERR, one for each pathway. Gibbs free energy changes for the elementary steps including zero point energies and entropies, and cell potential effects are estimated following the methodology introduced by Norskov et al.^{20,21}

The ΔG for the overall reaction ($\frac{1}{2}\text{O}_2 + \text{H}_2 \rightarrow \text{H}_2\text{O}$) is calculated to be 2.13 eV that makes the theoretical results off by about 14% (the experimental value is 2.5 eV) compared with experiments; this discrepancy has been attributed in part to the difficulties in modeling the O₂ electronic structure.²¹ The results shown below that introduce the electrode potential in the free energy profiles are based on the calculated ΔG for the overall reaction.

5.1. A Direct Pathway Mechanism. A simple mechanism associated with the *direct* pathway, where the O–O splits before the first hydrogenation, is summarized by eqs 3–5, and Figure 3 displays the ΔG profile for the cell at the equilibrium potential.



The surface with the highest d-band center and thus the most reactive one (Pd (111)) is the only one on which the current model predicts water dissociation (the reverse reaction to that shown in Figure 3) at the cell's equilibrium potential and at the studied oxygen coverage ($\theta = 0.25$). On the other hand, for Pt(111) at the equilibrium potential, at the oxygen coverage $\theta = 0.25$ and in the absence of water we find a slightly uphill path for water dissociation. Norskov et al.²⁰ calculations yield a thermodynamic barrier for water dis-

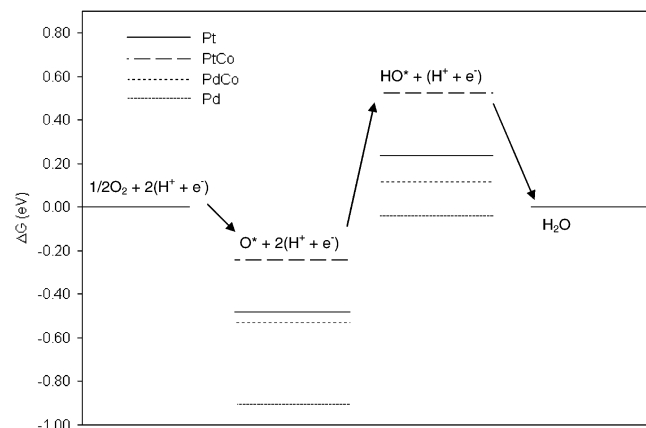
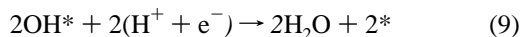
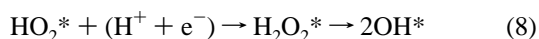
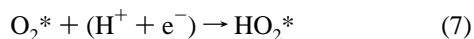


Figure 3. DFT calculated Gibbs free energy profile for a *direct* mechanism of the OERR on Pt, Pt_{0.75}Co_{0.25} and Pd_{0.75}Co_{0.25}, and Pd surfaces at the cell equilibrium potential.

sociation on Pt (111) at the cell equilibrium potential and $\theta = 0.5$, while the barrier becomes downhill at an unspecified low coverage; we assume (based on their largest cell size) that this corresponds to a value of $\theta = 0.167$. This is in good agreement with our results that predict a thermodynamic barrier for an oxygen coverage intermediate between those two cases.

The Pt surface of the Pt_{0.75}Co_{0.25} alloy shows ΔG values along the path that are above the Pt and Pd_{0.75}Co_{0.25} surfaces, while the ΔG values corresponding to the Pd surface which has the strongest bonds with the intermediates is below. Based solely on the data obtained on the profile the highest thermodynamic barrier for this reaction mechanism under the specific conditions (low oxygen coverage, no water) is likely to be located in the first hydrogenation (eq 4).

5.2. A Series Mechanism. The Gibbs free energy profile for a series mechanism indicated by the chemical eqs 6–9 is shown in Figure 4 at the cell equilibrium potential. In this mechanism we assume that H₂O₂ is unstable in all surfaces, and thus the result of the second hydrogenation reaction is its immediate dissociation yielding two adsorbed hydroxides.



At the cell equilibrium potential (1.23 V) there are a series of uphill thermodynamic barriers for the formation of water from hydrogen and oxygen. As in the first mechanism, the free energy profile under these conditions (low O coverage, no solvent) indicates that the highest thermodynamic barrier is the first hydrogenation (eq 7). Reactivity trends similar to the *direct* mechanism are found among the various surfaces, again following with the d-band center model. The difference in values for the thermodynamic barriers in both mechanisms is comparable signaling that both mechanisms might be active and operating in parallel.

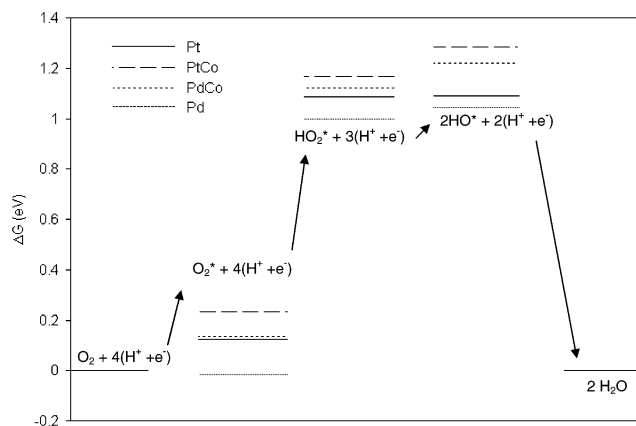


Figure 4. DFT calculated Gibbs free energy profile for a possible *series* mechanism of OERR in Pt, Pt_{0.75}Co_{0.25} and Pd_{0.75}Co_{0.25}, and Pd surfaces at the cell equilibrium potential.

6. Conclusions

Binding energies of oxygen electroreduction intermediates and free energy profiles for *direct* and *series* reaction mechanisms on (111) surfaces of Pt, Pd, Pd_{0.75}Co_{0.25}, and Pt_{0.75}Co_{0.25} indicate that the affinities toward the different ORR intermediates and reactivity trends on the studied surfaces follow the prediction of the d-band model. The study of the free energy profiles and the magnitude of the thermodynamic barriers in both mechanisms favors the hypothesis that the O₂ reduction mechanism to water might be operating in *parallel*. The highest thermodynamic barriers appear to be located in the first hydrogenation reaction for both mechanisms when the system is studied at conditions of 1/4 of a monolayer oxygen coverage and in the absence of water.

Acknowledgment. This work was supported by the Department of Energy, grant DE-FG02-05ER15729. This research used resources of the National Energy Research Scientific Computing Center, which is supported by the Office of Science of the U.S. Department of Energy under Contract No. DE-AC03-76SF00098. Supercomputer time granted by the DoD Major Shared Resource Center (ARL MSRC) is gratefully acknowledged.

References

- (1) Markovic, N. M.; Schmidt, T. J.; Stamenkovic, V.; Ross, P. N. Oxygen Reduction Reaction on Pt and Pt bimetallic Surfaces: A Selective Review. *Fuel Cells* **2001**, *1*, 105–116.
- (2) Toda, T.; Igarashi, H.; Uchida, H.; Watanabe, M. Enhancement of the Electroreduction of Oxygen on Pt Alloys with Fe, Ni and Co. *J. Electrochem. Soc.* **1999**, *146*, 3750–3756.
- (3) Stamenkovic, V.; Schmidt, T. J.; Ross, P. N.; Markovic, N. M. Surface segregation effects in electrocatalysis: kinetics of oxygen reduction on polycrystalline Pt₃Ni alloy surfaces. *J. Electroanal. Chem.* **2003**, *554–555*, 191–199.
- (4) Collman, J. P.; Wagenknecht, P. S.; Hutchison, J. E. Molecular Catalysts for Multielectron Redox Reactions of Small Molecules: The “Cofacial Metallodiporphyrin” Approach. *Angew. Chem., Int. Ed. Engl.* **1994**, *33*, 1537–1554.

- (5) Savadogo, O.; Lee, K.; Oishi, K.; Mitsushima, S.; Kamiya, N.; Ota, K.-I. New palladium alloys catalyst for the oxygen reduction reaction in an acid medium. *Electrochem. Commun.* **2004**, *6*, 105–109.
- (6) Shao, M. H.; Sasaki, K.; Adzic, R. R. Pd–Fe nanoparticles as electrocatalysts for oxygen reduction. *J. Am. Chem. Soc.* **2006**, *128*, 3526–3527.
- (7) Fernandez, J. L.; Walsh, D. A.; Bard, A. J. Thermodynamic Guidelines for the Design of Bimetallic Catalysts for Oxygen Electroreduction and Rapid Screening by Scanning Electrochemical Microscopy. M–Co (M: Pd, Ag, Au). *J. Am. Chem. Soc.* **2005**, *127*, 357–365.
- (8) Lee, K.; Savadogo, O.; Ishihara, A.; Mitsushima, S.; Kamiya, N.; Ota, K. Methanol-Tolerant Oxygen Reduction Electrocatalyst Based on Pd-3D Transition Metal Alloys for Direct Methanol Fuel Cell. *J. Electrochem. Soc.* **2006**, *153*, A20–A24.
- (9) Xu, Y.; Ruban, A.; Mavrikakis, M. Adsorption and Dissociation of O₂ on Pt–Co and Pt–Fe Alloys. *J. Am. Chem. Soc.* **2003**, *126*, 4717–4725.
- (10) Roques, J.; Anderson, A. B. Electrode Potential Dependence Stages in OHads Formation on the Pt3Cr Alloy (111) Surface. *J. Electrochem. Soc.* **2004**, *151*, E340–E347.
- (11) Balbuena, P. B.; Altomare, D.; Vadlamani, N.; Bingi, S.; Agapito, L. A.; Seminario, J. M. Adsorption of O, OH, and H₂O on Pt-Based Bimetallic Clusters Alloyed with Co, Cr, and Ni. *J. Phys. Chem. A* **2004**, *108*, 6378–6384.
- (12) Wang, Y.; Balbuena, P. B. Design of oxygen reduction bimetallic catalysts: Ab-initio derived thermodynamic guidelines. *J. Phys. Chem. B* **2005**, *109*, 18902–18906.
- (13) Panchenko, A.; Koper, M. T. M.; Shubina, T. E.; Mitchell, S. D.; Roduner, E. Ab Initio Calculations of Intermediates of Oxygen Reduction on Low-Index Platinum Surfaces. *J. Electrochem. Soc.* **2004**, *151*, A2016–A2027.
- (14) Xu, Y.; Ruban, A. V.; Mavrikakis, M. Adsorption and dissociation of O₂ on Pt–Co and Pt–Fe alloys. *J. Am. Chem. Soc.* **2004**, *126*, 4717–4725.
- (15) Adzic, R. R.; Wang, J. X. Configuration and site of O₂ adsorption on the Pt(111) electrode surface. *J. Phys. Chem. B* **1998**, *102*, 8988–8993.
- (16) Wang, J. X.; Markovic, N. M.; Adzic, R. R. Kinetic analysis of oxygen reduction on Pt(111) in acid solutions: Intrinsic kinetic parameters and anion adsorption effects. *J. Phys. Chem. B* **2004**, 4127–4133.
- (17) Paulus, U. A.; Wokaum, A.; Scherer, G. G.; Schmidt, T. J.; Stamenkovic, V.; Markovic, N. M.; Ross, P. N. Oxygen reduction on high surface area Pt-based alloy catalyst in comparison to well-defined bulk alloy electrodes. *Electrochim. Acta* **2002**, *47*, 3787–3798.
- (18) Hammer, B.; Norskov, J. K. Electronic factors determining the reactivity of metal surfaces. *Surf. Sci.* **1995**, *343*, 211–220.
- (19) Chorkendorff, I.; Niemantsverdriet, J. W. *Concepts of Modern Catalysis and Kinetics*; Wiley-VCH: 2003.
- (20) Norskov, J. K.; Rossmeisl, J.; Logadottir, A.; Lindqvist, L. Origin of the Overpotential for Oxygen Reduction at a Fuel-Cell Cathode. *J. Phys. Chem. B* **2004**, *108*, 17886–17892.
- (21) Rossmeisl, J.; Logadottir, A.; Norskov, J. K. Electrolysis of water on (oxidized) metal surfaces. *Chem. Phys.* **2005**, *319*, 178–184.
- (22) Vanderbilt, D. Soft Self-Consistent Pseudopotentials in a Generalized Eigenvalue Formalism. *Phys. Rev. B* **1990**, *41*, 7892.
- (23) Vanderbilt, D. Vanderbilt Ultra-Soft Pseudopotential Site. <http://www.physics.rutgers.edu/~dhv/uspp/> (accessed on July 19, 2006).
- (24) Marzari, N.; Vanderbilt, D.; De Vita, A.; Payne, M. C. Thermal Contraction and Disordering of the Al (110) Surface. *Phys. Rev. Lett.* **1999**, *82*, 3296–3299.
- (25) Broyden, C. G. The Convergence of a Class of Double-Rank Minimization Algorithms 2. The New Algorithm. *J. Inst. Math. Appl.* **1970**, *6*, 222–231.
- (26) Fletcher, R. A. A new approach to variable metric algorithms. *Comput. J.* **1970**, *13*, 317–322.
- (27) Goldfarb, D. A family of variable-metric methods derived by variational means. *Math. Comput.* **1970**, *24*, 23–26.
- (28) Shanno, D. F. Conditioning of quasi-Newton methods for function minimization. *Math. Comput.* **1970**, *24*, 647–656.
- (29) Scandolo, S.; Giannozzi, P.; Cavazzoni, C.; de Gironcoli, S.; Pasquarello, A.; Baroni, S. First-principles codes for Computational Crystallography in the Quantum-ESPRESSO package. *Z. Kristallogr.* **2005**, *220*, 574–579.
- (30) Humphrey, W.; Dalke, A.; Schulten, K. VMD – Visual Molecular Dynamics. *J. Mol. Graphics* **1996**, *14*, 33–38.
- (31) Wentzcovitch, R. M.; Martins, J. L.; Price, G. D. Ab Initio Molecular Dynamics with Variable Cell Shape: Application to MgSiO₃. *Phys. Rev. Lett.* **1993**, *70*, 3947–3950.
- (32) Alexandre, S. S.; Mattesini, M.; Soler, J. M.; Yndurain, F. Comment on “Magnetism in Atomic-Size Palladium Contacts and Nanowires”. *Phys. Rev. Lett.* **2006**, *96*, 079701.
- (33) Eichler, A.; Hafner, J. Molecular Precursors in the Dissociative Adsorption of O₂ on Pt (111). *Phys. Rev. Lett.* **1997**, *79*, 4481–4484.
- (34) Grob, A.; Eichler, A.; Hafner, J.; Mehl, M. J.; Papaconstantopoulos, D. A. Unified picture of the molecular adsorption process: O₂/Pt(111). *Surf. Sci.* **2003**, *539*, L542–L548.
- (35) Puglia, C.; Nilsson, A.; Hernnas, B.; Karis, O.; Bennich, P.; Martensson, N. Physisorbed, Chemisorbed and Dissociated O₂ on Pt(111) Studied by Different Core Level Spectroscopy Methods. *Surf. Sci.* **1995**, *342*, 119.
- (36) Jacob, T.; Muller, R. P.; Goddard, W. A., III Chemisorption of Atomic Oxygen on Pt(111) from DFT Studies of Pt-Clusters. *J. Phys. Chem. B* **2003**, *107*, 9465–9476.
- (37) Suresh, S. J.; Naik, V. M. Hydrogen bond thermodynamic properties of water from dielectric constant data. *J. Chem. Phys.* **2000**, *113*, 9727–9732.
- (38) Michaelides, A.; Hua, P. A density functional theory study of hydroxyl and the intermediate in the water formation reaction on Pt. *J. Chem. Phys.* **2001**, *114*, 513–519.
- (39) Wroblowa, H. S.; Yen-Chi-Pan; Razumney, G. Electroreduction of Oxygen a New Mechanistic Criterion. *J. Electroanal. Chem.* **1976**, *69*, 195–201.